RSC Advances

ROYAL SOCIETY OF CHEMISTRY

PAPER

View Article Online
View Journal | View Issue

Check for updates

Cite this: *RSC Adv.*, 2026, **16**, 13875

SCAPS-1D simulation of lead-free perovskite solar cells: performance analysis and optimization

Raghad Nasser S. Alghamdi, Elsayed Ibrahim Shalaan and Ahmed Obaid M. Alzahrani *

Received 2nd November 2025
Accepted 5th March 2026

DOI: 10.1039/d5ra08437g

rsc.li/rsc-advances

Halide double perovskites have recently emerged as stable and non-toxic substitutes for lead-based materials in optoelectronic applications. Among these materials, Cs_2PtI_6 is distinguished by its high absorption coefficient, a bandgap (E_g) of 1.37 eV, and a long minority carrier diffusion length, due to its lower recombination rate, indicating an advantageous carrier lifetime and effective charge collection. Additionally, the appropriate selection of charge transport materials significantly enhances power conversion efficiency and overall performance. This work presents a theoretical evaluation of an n-i-p configured solar cell (FTO/SnO_2/Cs_2PtI_6/Spiro-OMeTAD/C), performed using the SCAPS-1D simulation tool. To optimize device performance, several parameters are systematically adjusted, including the thickness of the absorber layer, defect densities at the bulk and interface, the electrical resistances (series and shunt), and the selection of a suitable back contact material. Under standard conditions, the optimized device shows a remarkable power conversion efficiency (PCE) of 25.7%. Upon optimization, the spectral response shows a high quantum efficiency (QE) of 97.5% across the wavelength range. These results provide a significant theoretical understanding for improving the performance and design of perovskite solar cells.

1 Introduction

Perovskite solar cells (PSCs) are acknowledged as a potential photovoltaic technology owing to their elevated power conversion efficiency (PCE) and lower production costs.[1] Lead halide perovskites exhibit outstanding light and electrical properties, including high solar energy conversion efficiency, largely due to their strong optical absorption.[2] In addition, their tunable band gap allows precise control of the absorption spectrum through compositional engineering.[3,4] Moreover, their solution processability renders them promising candidates for solar applications.[5]

Despite the outstanding performance demonstrated by these materials, lead halide perovskites still face critical challenges that limit their long-term stability and practical application.[6,7] Thermal instability presents a significant challenge, as high temperatures can compromise the perovskite structure.[7] For instance, methylammonium lead iodide ($CH_3NH_3PbI_3$), a widely researched perovskite absorber, is particularly vulnerable to thermal degradation, which leads to decomposition of the organic component and a loss of the perovskite crystal structure, ultimately resulting in diminished optoelectronic properties and impaired device performance.[8] This remarkable rise of lead halide perovskite solar cells has been tempered by legitimate environmental and regulatory concerns regarding lead toxicity.[9] While lead-based devices now exceed 26% power conversion efficiency (PCE), the scientific community faces an urgent chemical challenge to design non-toxic alternatives that preserve favorable optoelectronic properties while overcoming intrinsic instability mechanisms rooted in molecular chemistry.

Considering these concerns, researchers are investigating lead-free perovskite materials that preserve the advantageous characteristics of conventional perovskites while addressing their inherent limitations.[10] One such promising candidate is Cs_2PtI_6, a lead-free vacancy-ordered double perovskite (A_2BX_6).[11] It crystallizes in a face-centered cubic structure ($Fm\bar{3}m$), consisting of isolated $[PtI_6]^{2-}$ octahedra separated by 12-coordinated Cs^+ ions; a tolerance factor close to unity supports cubic phase stability.[12] It has a narrow optical bandgap (E_g) of approximately 1.37 eV.[13] Experimentally, solution-processed Cs_2PtI_6 thin films exhibit a high absorption coefficient ($\sim 4 \times 10^5$ cm^{-1}) and long minority carrier lifetimes exceeding 2 μs, along with enhanced ambient and thermal stability.[14] Furthermore, Cs_2PtI_6 has been reported to exhibit pronounced chemical stability under harsh environments, including resistance to degradation across a wide pH range.[15]

The performance of PSCs is influenced by various factors, including device architecture,[16] charge transport layers,[17] and electrode materials.[18] The selection of charge transport layers depends on several factors, including high electrical conductivity for efficient carrier extraction,[19] sufficient transparency to reduce optical losses,[20] proper energy band alignment for selective transport, and

---

Department of Physics, Faculty of Science, King Abdulaziz University, Jeddah 21589, Saudi Arabia. E-mail: aualzahrani@kau.edu.sa

chemical stability with both the perovskite absorber and the electrodes.[21] Electron transport materials have shown significant progress, with metal oxides such as TiO_2 and SnO_2 being widely used due to their effectiveness in extracting electrons.[22]

Regarding hole transport layers, a wide range of materials has been investigated in perovskite solar cells. Inorganic materials, such as NiO_x, CuI, and MoO_x, offer high chemical stability and low cost; however, their primary limitation is poor hole extraction capability.[23,24] In contrast, organic materials like poly(3,4-ethylenedioxythiophene):poly(styrene sulfonate) (PEDOT:PSS) and 2,2′,7,7′-Tetrakis(*N*,*N*-di-*p*-methoxyphenylamine)-9,9′-spirobifluorene (Spiro-OMeTAD) provide efficient hole extraction, thereby enhancing power conversion efficiency;[25] however, they suffer from instability due to their sensitivity to moisture and oxygen.[23,24] One effective approach to address the instability of organic hole transport layers is doping.[26] For instance, a study by Xiaobing Wang *et al.*[27] demonstrated that adding V_2O_5 to Spiro-OMeTAD improved its stability, allowing the solar cell to retain 90% of its original efficiency after 30 days of exposure to 40% humidity.

For Cs_2PtI_6-based perovskite solar cells, efficient charge separation and transport are crucial for enhancing device performance. Nevertheless, experimental studies on this material remain limited. In this work, a numerical simulation analysis is performed to investigate the effects of absorber thickness, bulk and interfacial defect densities, series and shunt resistances, and back-contact work function, aiming to provide valuable insights for future experimental research.

2 Materials and methodology

2.1 SCAPS-1D numerical simulation

The present work involves one-dimensional modeling of photovoltaic cells performed using the SCAPS-1D simulator (version 3.3.11), developed by Burgelman *et al.* at Ghent University.[28,29] This simulation software is widely used to analyze the performance of solar cell structures under various operating conditions. SCAPS-1D supports the simulation of seven layers, including front and back contacts, and offers high flexibility for defining a wide range of physical and electrical parameters. The simulator allows the evaluation of several key characteristics, including current–voltage (*J*–*V*) behavior, AC responses such as capacitance–frequency (*C*–*F*) and capacitance–voltage (*C*–*V*), power conversion efficiency (PCE), fill factor (FF), short-circuit current density (J_{sc}), open-circuit voltage (V_{oc}), and quantum efficiency (QE).

The simulations' fundamental equations are Poisson's eqn (1), the continuity equations for holes and electrons (2), and the drift–diffusion transport equations for charge carriers (3) and (4).[30,31]

$$\frac{d^2\psi}{dx^2} = \frac{e}{\varepsilon_o\varepsilon_r}\left[p_{(x)} - n(x) + N_D - N_A + \rho_p - \rho_n\right] \tag{1}$$

where ψ represents the electrostatic potential, n and p denote electron and hole concentrations, ε_0 and ε_r are the vacuum and relative permittivities, N_D and N_A refer to donor and acceptor doping densities, and ρ_n and ρ_p correspond to the distribution of electrons and holes.

$$\frac{dJ_p}{dx} = \frac{dJ_n}{dx} = G - R \tag{2}$$

Here, G and R represents the generation and recombination rate. The current densities of holes and electrons are indicated by J_p and J_n, respectively.

$$J_n = \mu_n n\frac{d\varphi}{dx} + D_n\frac{dn}{dx} \tag{3}$$

$$J_p = \mu_p p\frac{d\varphi}{dx} + D_p\frac{dp}{dx} \tag{4}$$

where μ_n, μ_p, D_n, and D_p denote the hole and electron mobilities and diffusion coefficients, respectively.

The optical absorption coefficient in SCAPS can be calculated using several different methods. In this study, we used eqn (5) embedded in the software, known as the Tauc law.[32]

$$\alpha(\lambda) = \left(A + \frac{B}{hv}\right)\sqrt{hv - E_g} \tag{5}$$

E_g and hv are the band gap of the material and the photon energy, respectively. A and B these are the model parameters.

The relationship between V_{oc}, J_{sc}, and FF can be described using the following eqn (6):

$$V_{oc} = \frac{k_B T}{q}\ln\left(\frac{J_{sc}}{J_0} + 1\right) \tag{6}$$

The J_0 is the saturation current density, given by eqn (7):

$$J_0 = qN_vN_c\left[\frac{1}{N_A}\left(\frac{D_n}{\tau_n}\right)^{\frac{1}{2}} + \frac{1}{N_D}\left(\frac{D_p}{\tau_p}\right)^{\frac{1}{2}}\right]e^{-\frac{E_g}{k_B T}} \tag{7}$$

N_c and N_V represent the effective density of states for electrons and holes, respectively, k_B is the Boltzmann constant, and T is the temperature.

The fill factor (FF) is the ratio between V_{max},J_{max} (the voltage and current at the maximum power point, respectively), and the theoretical power V_{oc},J_{sc}, as shown in eqn (8).

$$FF = \frac{V_{max} \times J_{max}}{V_{oc} \times J_{sc}} \tag{8}$$

Finally, the PCE of the solar device is calculated as follows:

$$PCE = \frac{V_{oc} \times J_{sc} \times FF}{P_{in}} \tag{9}$$

where P_{in} denotes the optical input power of solar radiation.

2.2 Perovskite solar cell structure

Fig. 1(a) illustrates the layered structure of the proposed device, which consists of FTO/SnO_2/Cs_2PtI_6/Spiro-OMeTAD/Carbon. Fig. 1(b) shows the corresponding energy level alignment between these layers, indicating a well-matched configuration that facilitates selective charge transport. This energy alignment allows only one type of charge carrier (electrons or holes) to pass in the desired direction. In contrast, the energy barriers

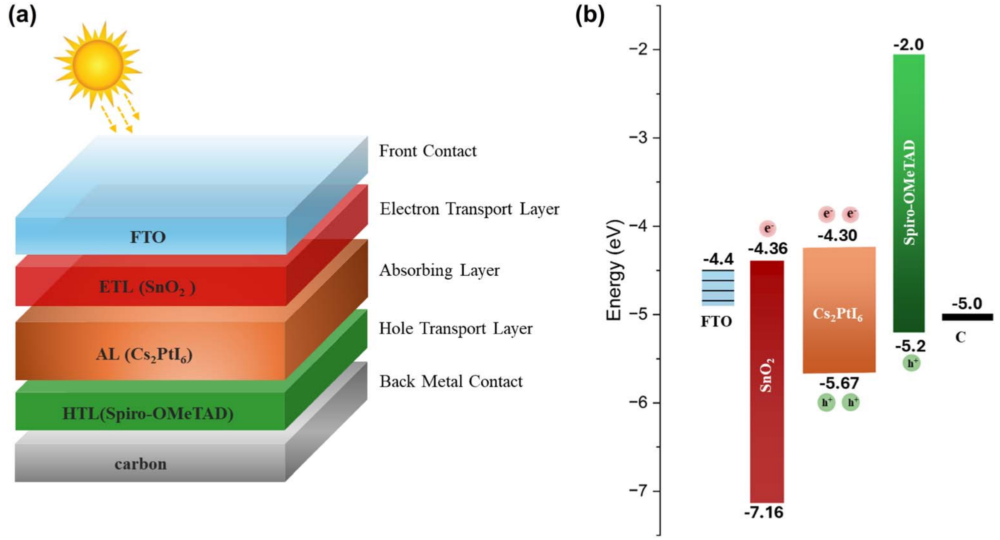

Fig. 1 (a) Schematic structure of the lead-free Cs_2PtI_6 perovskite solar cell device, and (b) the corresponding energy band diagram.

Table 1 Input parameters for materials used in the device

Input parameters	FTO	ETL (SnO_2)	Cs_2PtI_6	HTL (Spiro-OMeTAD)
Thickness, d (nm)	150	40	200	100
Bandgap, E_g (eV)	3.5	2.8	1.37	3
Electron affinity, x	4	4	4.3	2.2
Permittivity, ε_r	9	34.8	4.8	3
Electron mobility, μ_n ($cm^2 V^{-1} s^{-1}$)	20	20	62.6	2.1×10^{-3}
Hole mobility, μ_p ($cm^2 V^{-1} s^{-1}$)	10	10	62.6	2.16×10^{-3}
Effective density of states at CB, N_c (cm^{-3})	2.2×10^{18}	2.4×10^{18}	3.0×10^{14}	2.2×10^{18}
Effective density of states at VB, N_v (cm^{-3})	1.8×10^{19}	1.8×10^{19}	1.0×10^{17}	1.8×10^{19}
Density of n-type doping, N_D (cm^{-3})	1×10^{19}	1.0×10^{18}	1.0×10^{15}	0
Density of p-type doping, N_A (cm^{-3})	0	0	1.0×10^{12}	1.0×10^{19}
Defect density, N_t (cm^{-3})	—	1.0×10^{15}	1.0×10^{17}	1.0×10^{15}
Capture cross-section electron (cm^2)	—	2×10^{-14}	1.0×10^{-15}	1.0×10^{-15}
Capture cross-section holes (cm^2)	—	2×10^{-14}	1.0×10^{-15}	1.0×10^{-15}
References	33	34	11	35

Table 2 Defect parameters of the ETL/perovskite and perovskite/HTL interfaces

	Defect type	Capture cross: section electrons/holes [cm^2]	Energetic distribution	Reference for defect energy level, E_t	Energy with respect to a reference (eV)	Total defect density (cm^{-2})
ETL/Cs_2PtI_6	Neutral	1.0×10^{-18}	Single	Above the highest E_v	0.600	1.00×10^{13}
HTL/Cs_2PtI_6	Neutral	1.0×10^{-18}	Single	Above the highest E_v	0.600	1.00×10^{13}

effectively block the opposite type of charge carrier. As a result, charge recombination is suppressed, thereby improving photovoltaic performance. Table 1 presents the input parameters for materials, obtained from the literature. The work functions of the front (FTO) and back (carbon) contacts are 4.4 eV and 5.0 eV, respectively. The thermal velocity of holes and electrons is 1×10^7 at 300 K. Table 2 lists the defect parameters of ETL/Cs_2PtI_6 and Cs_2PtI_6/HTL interfaces. All simulations were conducted under AM1.5G illumination, with an input power of 1000 W m^{-2} and a working temperature of 300 K.

3 Results and discussion

3.1 Effect of absorbing layer thickness and defect density

The active perovskite material plays a vital role in device efficiency and stability, as its thickness and defect density directly affect light absorption, charge carrier dynamics, and recombination processes.[36–38] In this work, we varied both the thickness and intrinsic defect concentration of the absorber layer to evaluate the performance of the fabricated devices.

Table 3 shows the variation of diffusion length (L) and carrier lifetime (τ) with increasing defect concentration in the

Table 3 Variation of charge carrier diffusion length and lifetime with different defect concentration values

N_t (cm^{-3})	$L_{n,p}$ (nm)	$\tau_{n,p}$ (s)
1×10^{14}	13 000	1.0×10^{-6}
1×10^{15}	4000	1.0×10^{-7}
1×10^{16}	1300	1.0×10^{-8}
1×10^{17}	400	1.0×10^{-9}
1×10^{18}	130	1.0×10^{-10}
1×10^{19}	40	1.0×10^{-11}
1×10^{20}	13	1.0×10^{-12}

absorbing layer. As defect concentration increases, defects act as trap states that capture charge carriers, leading to decreased diffusion length and carrier lifetime, increased charge recombination, and reduced charge extraction from the absorber layer.

The diffusion length (L) in the device is calculated as the square root of the multiplication of the diffusion coefficient (D) and the carrier lifetime (τ), which denotes the typical duration before a charge recombination as shown in eqn (10), expressed in centimeters. The diffusion coefficient (D) is defined in eqn (11) in cm^2 s^{-1}.

$$L = \sqrt{D\tau} \tag{10}$$

where

$$D = \frac{\mu k_B T}{q} \tag{11}$$

Here, μ is the charge mobility for both electrons and holes in the Cs_2PtI_6 material (62.6 cm^2 V^{-1} s^{-1}), T is the temperature (set to 300 K in this simulation), and q is the elementary charge (1.6×10^{-19} C).

The expression for carrier lifetime (τ) is presented in eqn (12)

$$\tau = \frac{1}{\sigma V_{th} N_t} \tag{12}$$

where, σ represents the capture cross-section in material, which is 1.0×10^{-15} cm^2 and V_{th} is a thermal velocity (1×10^7 cm s^{-1}).[39]

Fig. 2 presents the impact of bulk defect density and the thickness of the Cs_2PtI_6 on the performance of PSCs. In this study, the defect density is varied over a wide range, from 10^{14} to 10^{20} cm^{-3}, to investigate how increasing the trap density influences key device parameters. Although defect density around 10^{14}–10^{15} cm^{-3} are typically considered optimal for performance, previous reports suggest that experimental values are often much higher, commonly in the range of 10^{16}–10^{17} cm^{-3}.[40,41] Therefore, a realistic upper limit is also included to understand how typical defect conditions affect device behavior.

Based on this hypothesis, we select $N_t = 10^{17}$ cm^{-3} as a representative value to investigate the effect of changing the Cs_2PtI_6 thickness from 300 nm to 1000 nm. Fig. 2(f) shows that as the thickness increases, the short-circuit density (J_{sc}) gradually increases as a result of improved light absorption, which enhances the generation of electron–hole pairs. However, when the thickness exceeds 400 nm, J_{sc} gradually decreases due to increased recombination within the absorber layer. This is attributed to the perovskite layer thickness exceeding the charge diffusion length, thereby reducing charge collection efficiency.

The open-circuit voltage (V_{oc}) in Fig. 2(g) increases from 100 to 200 nm, then remains constant, indicating a stable built-in electric field across the device.

Fig. 2(e and h) demonstrate that both the fill factor (FF) and power conversion efficiency (PCE) reach their maximum values

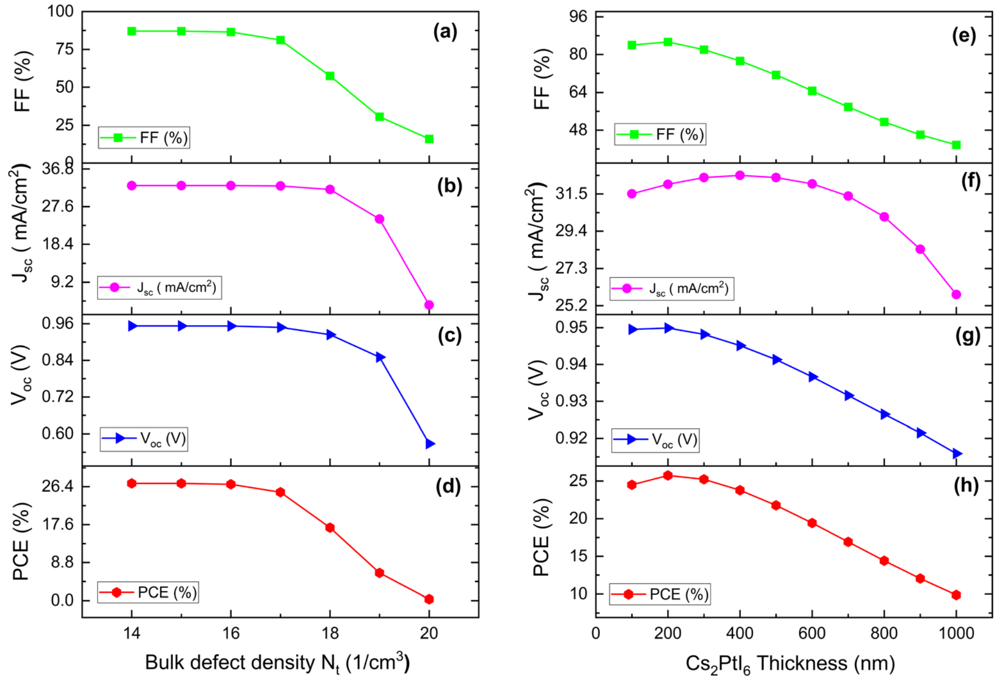

Fig. 2 Effect of Cs_2PtI_6 bulk defect density (N_t) and absorber thickness in the perovskite material.

Table 4 Work function of different back metal contacts[33]

Back metal	Cu	Ni	Ag	Fe	Go	C
Work function (eV)	4.53	4.61	4.74	4.81	4.9	5

at 200 nm, beyond which both parameters steadily decline. This reduction in performance is mainly attributed to enhanced carrier recombination within thicker absorber layers, as described by the Shockley–Read–Hall (SRH) mechanism. The SRH recombination rate is expressed by eqn (13).[42]

$$R_{\mathrm{SRH}} = \frac{np - n_i^{\,2}}{\tau_{\mathrm{nr}}(n + p)} \tag{13}$$

where n and p represent electron and hole densities, n_i is the intrinsic carrier concentration, and τ_nr is the non-radiative carrier lifetime.

The ideal thickness of the perovskite layer is achieved by balancing light absorption and charge diffusion length in planar PSCs. High achievements require that the charge diffusion length be longer than the perovskite layer thickness.[43–45] In this study, a thickness of 200 nm is selected, corresponding to a power conversion efficiency of 25.7% at a defect density of 10^{17} cm^{-3}, with a calculated diffusion length of 400 nm, as illustrated in Table 4.

3.2 Effect of interface defect density

The formation of structural defects during solar cell fabrication results in interfacial defects.[46] Differences in thermal expansion behavior and chemical compatibility between adjacent layers can induce interfacial stress and unfavorable interfacial interactions, leading to the formation of defect and trap states.[47,48] These interfacial defects act as recombination centers, limiting efficient charge extraction.[48]

Defects at the HTL/perovskite interface act as trap states that capture holes, leading to nonradiative recombination and charge accumulation, ultimately reducing the quasi-Fermi level splitting and lowering V_oc.[49,50] In contrast, defects at the ETL/perovskite interface reduce J_sc by trapping electrons and limiting their collection.[50,51] This reduction agrees with the study by Chouhan *et al.*[52] which found that increasing the defect density at the HTL interface decreases V_oc from 1.34 V to 0.72 V. Similarly, increasing the defect density at the ETL interface decreases J_sc from 24.2 to 6.5 mA cm^{-2}, leading to a significant reduction in efficiency in both cases.

In this work (as shown in Fig. 3(a–h)), a similar pattern was observed when the defect density varied from 10^{12} to 10^{18} cm^{-2}. At the HTL/perovskite interface, the increase in interface defect density leads to a decrease in the open-circuit voltage (V_oc) from 1.00 V to 0.70 V. Consequently, the power conversion efficiency (PCE) drops from 27.19% to 18.62%. The short-circuit current density (J_sc) remains nearly constant at 31.7 mA cm^{-2} across all studied defect densities. Meanwhile, the fill factor (FF) initially rises to 85.38% at a defect density of 10^{13} cm^{-2}, then decreases at higher defect densities, indicating increased charge losses and recombination at the interface.

The ETL/perovskite interface has a lower effect on the defect density. The open-circuit voltage (V_oc) remains nearly constant at 0.94 V at all chosen defect densities. However, a gradual decrease in J_sc from 31.75 to 30.46 mA cm^{-2} resulted in a decline in efficiency from 25.7% to 22.4%. The fill factor (FF) remains almost unchanged within the lower defect range and begins to decrease only slightly at higher defect densities.

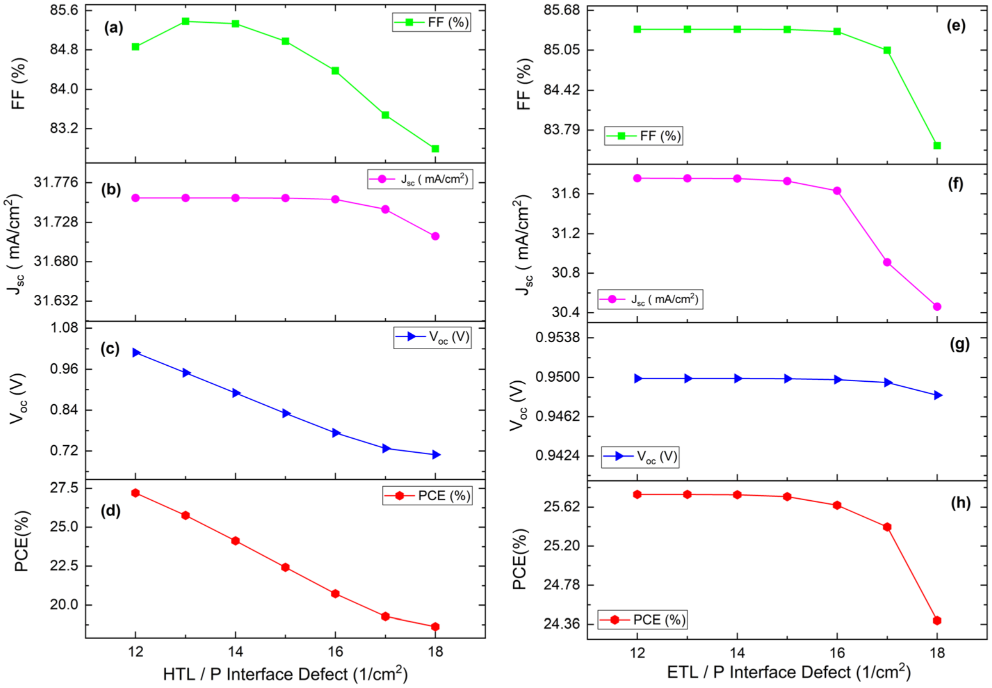

Fig. 3 Effect of interface defect density at HTL/perovskite and ETL/perovskite junctions on PCE, FF, V_oc, and J_sc.

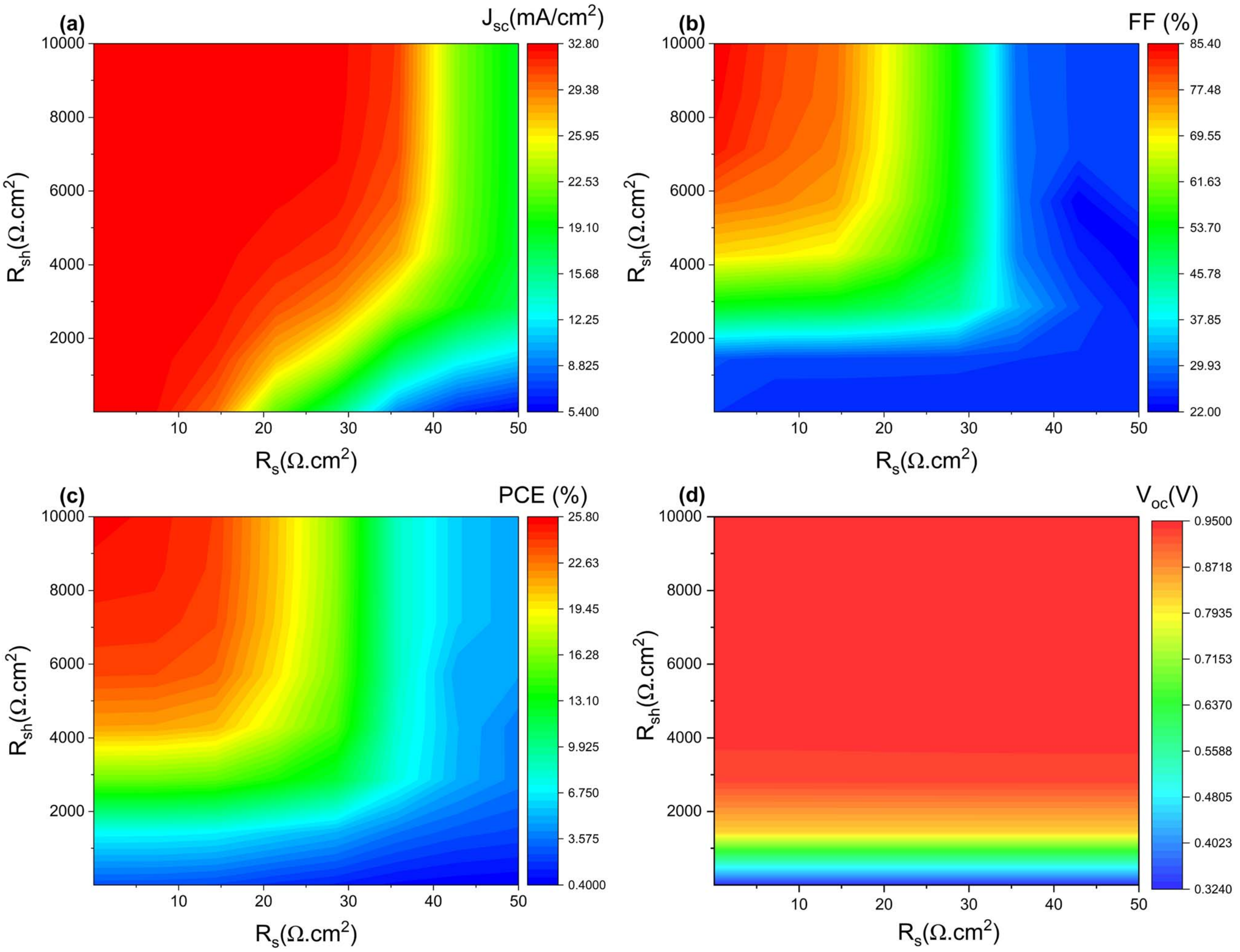

Fig. 4 Effect of series (R_s) and shunt (R_{sh}) resistances on J_{sc}, V_{OC}, FF, and PCE.

The above results demonstrate that defect density at both the HTL/perovskite and ETL/perovskite interfaces affects device performance, with a greater influence at the HTL interface. Therefore, interface defect passivation using materials with suitable functional groups that can chemically interact with and passivate interfacial trap states, or the introduction of interfacial layers, represents an effective strategy to reduce interfacial defects and improve the overall performance of perovskite solar cells.[53]

3.3 Effect of resistance on device parameters

The series resistance (R_s) and shunt resistance (R_{sh}) significantly impact solar cell performance. The resistive properties of the materials, interfaces, and electrical contacts within the device cause series resistance.[54,55] Shunt resistance is mainly associated with leakage pathways formed during fabrication, often arising from structural defects, non-uniform film formation, or pinholes within the perovskite layer and its interfaces.[54,56] In this study, we analyzed the effects of R_s and R_{sh} on device parameters by varying R_s from 0.01 to 50 Ω cm^2 and R_{sh} from 10 to 10 000 Ω cm^2. The following eqn (14) describes the impact that resistance has on the overall device behavior.[57]

$$I_{sc} = I_L + I_o\left(e^{\frac{V_{oc}q}{nKT}} - 1\right) - \frac{V_{oc} + I_{sc}R_s}{R_{sh}} \tag{14}$$

where I_{sc}, I_L, I_o denote the short-circuit current, the light-induced current, and the reverse saturation current, respectively, and n is the ideality factor.

Based on the above expression, an increase in series resistance reduces short-circuit current, negatively affecting both the fill factor and efficiency. Similarly, reducing the shunt resistance increases leakage, lowering the solar cell's overall performance.

Contour plots illustrate the corresponding photovoltaic parameters. The short-circuit current density (J_{sc}) in Fig. 4(a) decreases with increasing R_s, as the extraction of photogenerated charges becomes more challenging, particularly when R_s exceeds 30 Ω cm^2. Moreover, a reduction in R_{sh} increases current leakage through alternative pathways, thereby reducing current generation.

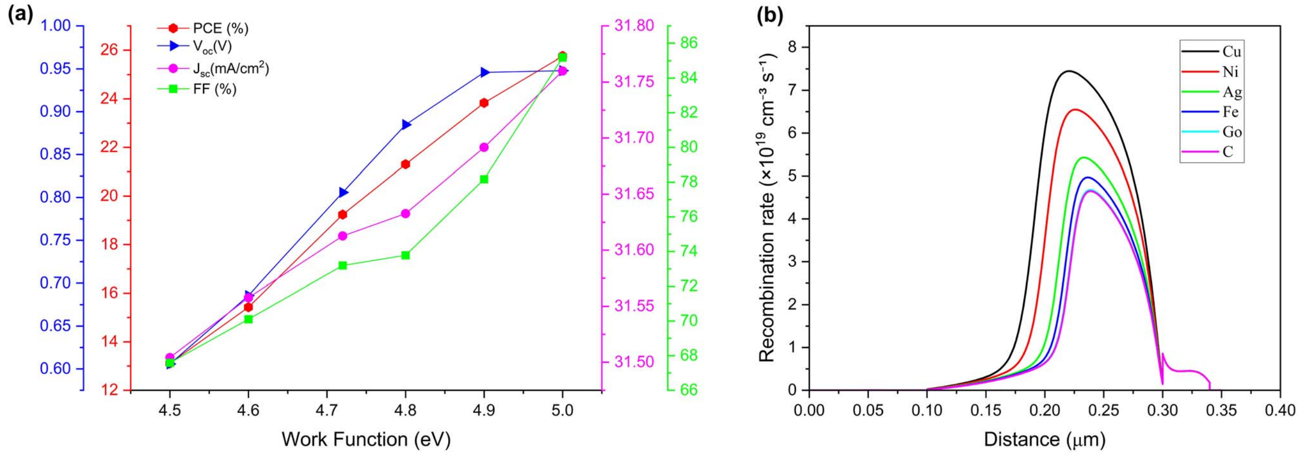

Fig. 5 Effect of back-contact work function on (a) J_{sc}, V_{oc}, FF, and PCE, and (b) recombination rate of the device.

In Fig. 4(d), R_s has a lesser impact on V_{oc} because it is measured under zero-current conditions. However, when R_{sh} decreases, particularly below 2000 Ω cm^2, V_{oc} drops significantly due to increased current leakage.

As shown in Fig. 4(b), the fill factor (FF) reaches nearly 85% when the series resistance is below 5 Ω cm^2, and the shunt resistance exceeds 6000 Ω cm^2. In contrast, FF drops significantly to around 22% when R_s exceeds 30 Ω cm^2, and R_{sh} falls below 2000 Ω cm^2.

Finally, Fig. 4(c) illustrates the power conversion efficiency (PCE), which directly reflects the combined effects of J_{sc}, V_{oc}, and FF. With optimal resistance values (low R_s and high R_{sh}), an efficiency of 25.8% can be achieved; however, deviations from these conditions substantially reduce performance.

3.4 Effect of back contact on device parameters

Back-contact metals function as electrodes for charge extraction, directly influencing device efficiency and stability. The choice of metal also affects key photovoltaic parameters due to variations in work function and interfacial properties with the perovskite absorber and hole transport layers.[58,59] Proper alignment between the metal work function and the HTL valence (HOMO) level enables efficient hole extraction through ohmic contact formation, whereas work function mismatch introduces interfacial barriers (blocking contacts) that increase resistance and degrade device performance, as experimentally demonstrated for various back metal electrodes.[60]

Accordingly, our study examined various metals as back contacts to investigate their impact on overall device performance. Table 4 summarizes the corresponding work function values.

Fig. 5(a) and (b) illustrate the effect of the back-contact work function on device performance and the recombination mechanism. A gradual improvement in performance is observed as the work function increases from 4.5 to 5.0 eV, reflected in improved key photovoltaic parameters. As shown in Fig. 5(a), the open-circuit voltage (V_{oc}) increases from 0.60 V to 0.94 V, while the fill factor (FF) improves from 67.5% to 85%, indicating enhanced interfacial contact quality.

In contrast, Fig. 5(b) demonstrates that this improvement is directly correlated with a reduction in the recombination rate. Devices with low-work-function back contacts exhibit higher recombination rates due to the formation of non-ohmic contacts, which hinder hole transport and cause carrier accumulation at the interface. With increasing work function, the energy-level alignment between the back contact and the hole-transport layer improves. This leads to more efficient charge extraction. As a result, the power conversion efficiency (PCE) increases significantly, reaching 25.7% when carbon is used as the back contact.

3.5 *J–V* characteristics and quantum efficiency

The current–voltage (*J–V*) characteristics and quantum efficiency (QE) spectrum are critical parameters for assessing the overall efficiency of a solar cell. The *J–V* curve indicates essential electrical parameters—short-circuit current density (J_{sc}), open-circuit voltage (V_{oc}), fill factor (FF), and power conversion efficiency (PCE), while the QE spectrum illustrates the device's spectral response and its capability to convert incident photons into photocurrent across various wavelengths. Fig. 6 shows the *J–V* and quantum efficiency (QE) curves. The *J–V* curve of the optimized device under AM1.5G illumination shows a J_{sc} of 31.75 mA cm^{-2}, a V_{oc} of 0.94 V, an FF of 85.38%, and a PCE of 25.7%. The results validate the efficiency of the implemented structural modifications in enhancing electrical performance.

The QE spectrum indicates that the device achieves a maximum quantum efficiency of approximately 97.5% over the 370–700 nm wavelength range. Beyond this region, the QE gradually decreases, reaching around 45% at 900 nm. This performance highlights the device's high capacity to capture solar energy.

In addition, the performance of any single-junction photovoltaic device is fundamentally constrained by the Shockley–Queisser (SQ) limit, which defines the theoretical upper bounds of key photovoltaic parameters under AM1.5G illumination.[61]

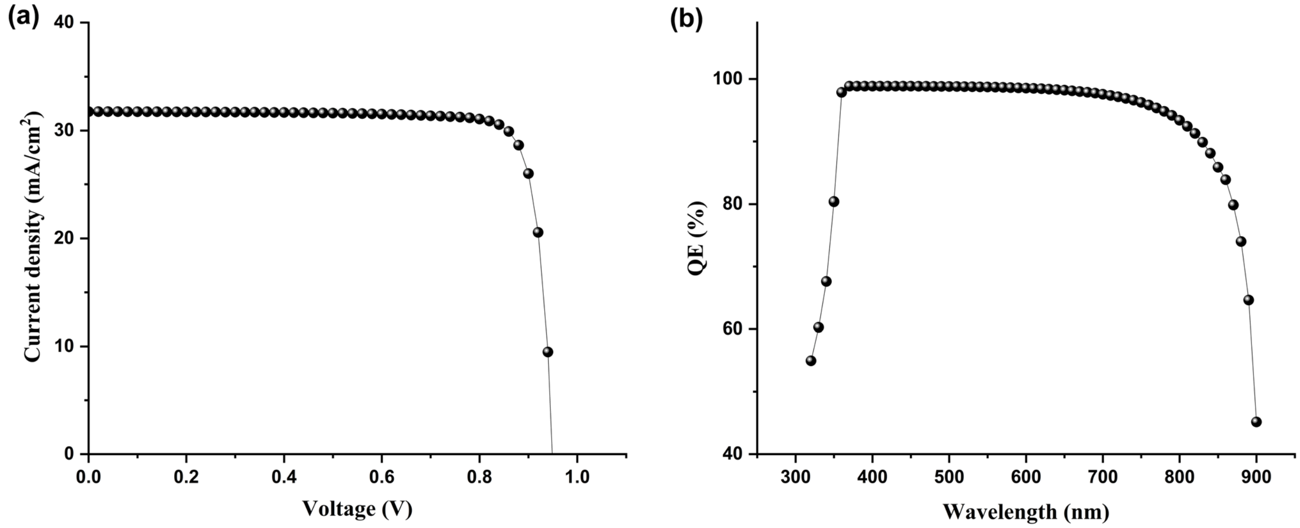

Fig. 6 (a) Current–voltage (*J*–*V*) characteristics and (b) quantum efficiency (QE) spectrum for the optimized perovskite solar cell.

For an absorber bandgap of approximately 1.37 eV, as in Cs_2PtI_6, the photovoltaic parameters are expected to lie within physically realistic theoretical ranges, while the maximum achievable power conversion efficiency approaches ~30%.[62] Accordingly, all simulated device parameters in this work were carefully examined to remain within these physical constraints, ensuring that the reported results represent a theoretical upper-limit performance rather than experimentally achievable values.

4 Conclusion

This study establishes a chemistry-driven optimization framework for lead-free Cs_2PtI_6 double perovskite solar cells, where photovoltaic performance emerges from deliberate control of chemical phenomena rather than geometric device tuning alone. Central to our approach is the recognition that key optoelectronic parameters – defect densities, energy level alignment, and interfacial recombination – are manifestations of underlying chemical processes: defect formation thermodynamics in the perovskite lattice, coordination chemistry at heterointerfaces, and surface functionalization of electrodes.

The selection of Cs_2PtI_6 as the absorber stems from its unique double perovskite chemistry, where the ordered arrangement of Pt^{2+}/Pt^{4+} in a rock-salt configuration within the $[PtI_6]^{4-}$ octahedral framework confers intrinsic stability against moisture-induced degradation – a critical chemical advantage over hybrid organic–inorganic perovskites.[13,15]

Our thickness optimization to 300 nm directly correlates with defect chemistry: at this dimension, the formation energies of deep-level chemical defects (particularly iodine vacancies V_I^+ and Pt–I antisite defects Pt_I) are minimized under iodine-rich synthesis conditions, suppressing Shockley–Read–Hall recombination pathways that originate from undercoordinated metal centers and halide vacancies. This thickness-dependent defect tolerance provides synthetic chemists with a target film morphology that balances crystallinity against defect proliferation during solution processing or vapor deposition.

Interfacial chemistry governs charge extraction efficiency at both electron- and hole-selective contacts. At the SnO_2/Cs_2PtI_6 interface, oxygen termination of SnO_2 creates Lewis acid–base interactions with undercoordinated I^- sites, passivating interfacial trap states that would otherwise arise from halide deficiency during film growth.

Similarly, the Spiro-OMeTAD/Cs_2PtI_6 junction benefits from methoxy group coordination to surface Pt centers, mitigating interfacial recombination through chemical passivation rather than mere energetic alignment. Most significantly, the carbon back contact was engineered to a work function of 5.0 eV *via* oxidative surface functionalization – introducing carbonyl and carboxyl groups that create interfacial dipoles through charge transfer with SpiroOMeTAD. This surface chemistry approach transforms an inert electrode into an active chemical component that suppresses hole accumulation and interfacial degradation.

These chemically informed modifications culminate in an optimized device ($FTO/SnO_2/Cs_2PtI_6$/SpiroOMeTAD/C) achieving 25.7% power conversion efficiency ($V_{oc} = 0.94$ V, $J_{sc} = 32.6$ mA cm^{-2}, FF = 80%) with near-unity external quantum efficiency (~97.5% across 300–900 nm). Critically, this performance arises from rational manipulation of chemical parameters – defect formation energetics tied to halide stoichiometry, interfacial coordination chemistry, and electrode surface functionalization – rather than empirical device tuning.

Accordingly, this work provides actionable design principles:

1. Targeting iodine-rich growth conditions to suppress vacancy-mediated recombination in Pt-based double perovskites;

2. Leveraging Lewis acid–base chemistry for interfacial defect passivation at metal oxide/perovskite junctions;

3. Employing controlled oxidative surface chemistry to tune carbon electrode work functions without noble metals.

By bridging defect thermodynamics, coordination chemistry, and surface science to device performance, this study offers a chemistry-centric roadmap for synthesizing stable, high-efficiency lead-free perovskites – positioning both materials chemistry and device engineering, as the foundation for next-generation photovoltaics.

Conflicts of interest

There are no conflicts to declare.

Data availability

Data for this article, (simulation parameters) are included in the article. The code for solar cell simulation (SCAPS 1D) can be found at https://scaps.elis.ugent.be/. The version of the code employed for this study is version SCAPS 3.3.11.

Acknowledgements

The authors would like to acknowledge the General Authority for Defense Development (GADD) in Saudi Arabia for funding this research through project number (GADD_2024_01_382).

References

1 N. Suresh Kumar and K. Chandra Babu Naidu, A review on perovskite solar cells (PSCs), materials and applications, *J. Materiomics*, 2021, **7**(5), 940–956, DOI: 10.1016/j.jmat.2021.04.002.

2 Y. T. Huang, S. R. Kavanagh, D. O. Scanlon, A. Walsh and R. L. Z. Hoye, Perovskite-inspired materials for photovoltaics and beyond—from design to devices, *Nanotechnology*, 2021, **32**(13), 132004, DOI: 10.1088/1361-6528/ABCF6D.

3 J. H. Noh, S. H. Im, J. H. Heo, T. N. Mandal and S. Il Seok, Chemical Management for Colorful, Efficient, and Stable Inorganic–Organic Hybrid Nanostructured Solar Cells, *Nano Lett.*, 2013, **13**(4), 1764–1769, DOI: 10.1021/NL400349B.

4 G. E. Eperon, S. D. Stranks, C. Menelaou, M. B. Johnston, L. M. Herz and H. J. Snaith, Formamidinium lead trihalide: a broadly tunable perovskite for efficient planar heterojunction solar cells, *Energy Environ. Sci.*, 2014, **7**(3), 982–988, DOI: 10.1039/C3EE43822H.

5 J. S. Manser, M. I. Saidaminov, J. A. Christians, O. M. Bakr and P. V. Kamat, Making and Breaking of Lead Halide Perovskites, *Acc. Chem. Res.*, 2016, **49**(2), 330–338, DOI: 10.1021/ACS.ACCOUNTS.5B00455.

6 N. K. Kim, *et al.*, Investigation of Thermally Induced Degradation in CH3NH3PbI3 Perovskite Solar Cells using In-situ Synchrotron Radiation Analysis, *Sci. Rep.*, 2017, **7**(1), 4645, DOI: 10.1038/s41598-017-04690-w.

7 B. Brunetti, C. Cavallo, A. Ciccioli, G. Gigli, and A. Latini, *On the Thermal and Thermodynamic (In) Stability of Methylammonium Lead Halide Perovskites OPEN*, 2016, DOI: 10.1038/srep31896.

8 B. Kammlander, *et al.*, Thermal degradation of lead halide perovskite surfaces, *Chem. Commun.*, 2022, **58**(97), 13523–13526, DOI: 10.1039/D2CC04867A.

9 Z. Yue, H. Guo, Y. Cheng, Z. Yue, H. Guo and Y. Cheng, Toxicity of Perovskite Solar Cells, *Energies*, 2023, **16**(10), 4007, DOI: 10.3390/EN16104007.

10 W. Chen, *et al.*, Investigation of Vacancy-Ordered Double Perovskite Halides A2Sn1−xTixY6 (A = K, Rb, Cs; Y = Cl, Br, I): Promising Materials for Photovoltaic Applications, *Nanomaterials*, 2023, **13**(20), 2744, DOI: 10.3390/NANO13202744.

11 M. K. Hossain, *et al.*, An extensive study on charge transport layers to design and optimization of high-efficiency lead-free Cs2PtI6-based double-perovskite solar cells: A numerical simulation approach, *Results Phys.*, 2024, **61**, 107751, DOI: 10.1016/j.rinp.2024.107751.

12 M. Faizan, *et al.*, Electronic and optical properties of vacancy ordered double perovskites A2BX6 (A = Rb, Cs; B = Sn, Pd, Pt; and X = Cl, Br, I): a first principles study, *Sci. Rep.*, 2021, **11**(1), 6965, DOI: 10.1038/s41598-021-86145-x.

13 S. Yang, *et al.*, Novel Lead-Free Material Cs $_2$ PtI $_6$ with Narrow Bandgap and Ultra-Stability for Its Photovoltaic Application, *ACS Appl. Mater. Interfaces*, 2020, **12**(40), 44700–44709, DOI: 10.1021/acsami.0c11429.

14 D. Schwartz, *et al.*, Air Stable, High-Efficiency, Pt-Based Halide Perovskite Solar Cells with Long Carrier Lifetimes, *Phys. Status Solidi RRL*, 2020, **14**(8), 2000182, DOI: 10.1002/PSSR.202000182.

15 M. Hamdan and A. K. Chandiran, Cs2PtI6 Halide Perovskite is Stable to Air, Moisture, and Extreme pH: Application to Photoelectrochemical Solar Water Oxidation, *Angew. Chem., Int. Ed.*, 2020, **59**(37), 16033–16038, DOI: 10.1002/ANIE.202000175.

16 T. Lemercier, L. Perrin, E. Planès, S. Berson and L. Flandin, A Comparison of the Structure and Properties of Opaque and Semi-Transparent NIP/PIN-Type Scalable Perovskite Solar Cells, *Energies*, 2020, **13**(15), 3794, DOI: 10.3390/EN13153794.

17 V. M. Le Corre, *et al.*, Charge Transport Layers Limiting the Efficiency of Perovskite Solar Cells: How To Optimize Conductivity, Doping, and Thickness, *ACS Appl. Energy Mater.*, 2019, **2**(9), 6280–6287, DOI: 10.1021/ACSAEM.9B00856.

18 J. Chung, *et al.*, Impact of Electrode Materials on Process Environmental Stability of Efficient Perovskite Solar Cells, *Joule*, 2019, **3**(8), 1977–1985, DOI: 10.1016/J.JOULE.2019.05.018.

19 M. Stolterfoht, *et al.*, Approaching the fill factor Shockley–Queisser limit in stable, dopant-free triple cation perovskite solar cells, *Energy Environ. Sci.*, 2017, **10**(6), 1530–1539, DOI: 10.1039/C7EE00899F.

20 N. Marinova, *et al.*, Light Harvesting and Charge Recombination in CH3NH3PbI3 Perovskite Solar Cells Studied by Hole Transport Layer Thickness Variation, *ACS Nano*, 2015, **9**(4), 4200–4209, DOI: 10.1021/ACSNANO.5B00447.

21 S. Zhang, *et al.*, Interface Engineering of Solution-Processed Hybrid Organohalide Perovskite Solar Cells, *ACS Appl. Mater.*

Interfaces, 2018, **10**(25), 21681–21687, DOI: 10.1021/ACSAMI.8B02503.

22 A. G. Mirea, *et al.*, Electron transporting bilayers for perovskite solar cells: Spray coating deposition of c-TiO2/m-SnO2-quantum dots, *Colloids Surf., A*, 2025, **705**, 135508, DOI: 10.1016/j.colsurfa.2024.135508.

23 H. D. Pham, *et al.*, Boosting inverted perovskite solar cell performance by using 9,9-bis(4-diphenylaminophenyl) fluorene functionalized with triphenylamine as a dopant-free hole transporting material, *J. Mater. Chem. A*, 2019, **7**(20), 12507–12517, DOI: 10.1039/C9TA01681C.

24 H. D. Pham, *et al.*, Low-Cost Alternative High-Performance Hole-Transport Material for Perovskite Solar Cells and Its Comparative Study with Conventional SPIRO-OMeTAD, *Adv. Electron. Mater.*, 2017, **3**(8), 1700139, DOI: 10.1002/aelm.201700139.

25 H. D. Pham, *et al.*, One step facile synthesis of a novel anthanthrone dye-based, dopant-free hole transporting material for efficient and stable perovskite solar cells, *J. Mater. Chem. C*, 2018, **6**(14), 3699–3708, DOI: 10.1039/C7TC05238C.

26 T. H. Schloemer, J. A. Christians, J. M. Luther and A. Sellinger, Doping strategies for small molecule organic hole-transport materials: impacts on perovskite solar cell performance and stability, *Chem. Sci.*, 2019, **10**(7), 1904–1935, DOI: 10.1039/C8SC05284K.

27 X. Wang, *et al.*, High performance and stable perovskite solar cells using vanadic oxide as a dopant for spiro-OMeTAD, *J. Mater. Chem. A*, 2019, **7**(21), 13256–13264, DOI: 10.1039/C9TA03351C.

28 M. Burgelman, P. Nollet and S. Degrave, Modelling polycrystalline semiconductor solar cells, *Thin Solid Films*, 2000, **361–362**, 527–532, DOI: 10.1016/S0040-6090(99)00825-1.

29 M. Burgelman, K. Decock, S. Khelifi and A. Abass, Advanced electrical simulation of thin film solar cells, *Thin Solid Films*, 2013, **535**(1), 296–301, DOI: 10.1016/J.TSF.2012.10.032.

30 N. K. Bansal, S. Mishra, H. Dixit, S. Porwal, P. Singh and T. Singh, Machine Learning in Perovskite Solar Cells: Recent Developments and Future Perspectives, *Energy Technol.*, 2023, **11**(12), 2300735, DOI: 10.1002/ENTE.202300735.

31 K. T. Arockiya-Dass, K. Sekar and L. Marasamy, Theoretical Insights of Degenerate ZrS2 as a New Buffer for Highly Efficient Emerging Thin-Film Solar Cells, *Energy Technol.*, 2023, **11**(9), 2300333, DOI: 10.1002/ENTE.202300333.

32 S. R. Al Ahmed, Investigation on the Performance Enhancement of Heterojunction SnS Thin-Film Solar Cell with a Zn3P2 Hole Transport Layer and a TiO2 Electron Transport Layer, *Energy Fuels*, 2023, **38**(2), 1462–1476, DOI: 10.1021/ACS.ENERGYFUELS.3C03719.

33 A. Amjad, S. Qamar, C. Zhao, K. Fatima, M. Sultan and Z. Akhter, Numerical simulation of lead-free vacancy ordered Cs_2PtI_6 based perovskite solar cell using SCAPS-1D, *RSC Adv.*, 2023, **13**(33), 23211–23222, DOI: 10.1039/D3RA04176J.

34 G. Meng, N. K. Elumalai, H. Mehdizadeh-Rad, K. S. Ram, D. D. Y. Setsoafia and D. Ompong, Investigating the Impact of Interfacial Layers on Device Performance of Highly Stable $Cs_2InBiBr_6$ Based Double Perovskite Solar Cells, *Adv. Theory Simul.*, 2024, **7**(2), 2300784, DOI: 10.1002/adts.202300784.

35 M. K. Hossain, *et al.*, Combined DFT, SCAPS-1D, and wxAMPS frameworks for design optimization of efficient Cs_2BiAgI_6-based perovskite solar cells with different charge transport layers, *RSC Adv.*, 2022, **12**(54), 34850–34873, DOI: 10.1039/D2RA06734J.

36 T. Ouslimane, L. Et-taya, L. Elmaimouni and A. Benami, Impact of absorber layer thickness, defect density, and operating temperature on the performance of MAPbI3 solar cells based on ZnO electron transporting material, *Heliyon*, 2021, **7**(3), e06379, DOI: 10.1016/j.heliyon.2021.e06379.

37 N. Shrivastav, J. Madan, M. K. A. Mohammed, M. K. Hossain and R. Pandey, $CsPbI_{3-}$ perovskite quantum dot solar cells: unlocking their potential through improved absorber layer characteristics and reduced defects, *Mater. Res. Express*, 2023, **10**(7), 075506, DOI: 10.1088/2053-1591/ace591.

38 M. S. Hanif, I. Qasim, M. I. Malik, M. F. Nasir, O. Ahmad and A. Rashid, Development of low-cost and high-efficiency solar modules based on perovskite solar cells for large-scale applications, *Heliyon*, 2024, **10**(4), e25703, DOI: 10.1016/j.heliyon.2024.e25703.

39 S. Z. Haider, H. Anwar, S. Manzoor, A. G. Ismail and M. Wang, A theoretical study for high-performance inverted p-i-n architecture perovskite solar cells with cuprous iodide as hole transport material, *Curr. Appl. Phys.*, 2020, **20**(9), 1080–1089, DOI: 10.1016/j.cap.2020.06.022.

40 N. K. Noel, *et al.*, Lead-free organic–inorganic tin halide perovskites for photovoltaic applications, *Energy Environ. Sci.*, 2014, **7**(9), 3061–3068, DOI: 10.1039/C4EE01076K.

41 M. Jiang, *et al.*, Observation of lower defect density in CH3NH3Pb(I,Cl)3 solar cells by admittance spectroscopy, *Appl. Phys. Lett.*, 2016, **108**(24), 243501, DOI: 10.1063/1.4953834/971674.

42 V. Ivian, *et al.*, Fullerene-C60 and PCBM as interlayers in regular and inverted lead-free PSCs using CH3NH3SnI3: an analysis of device performance and defect density dependence by SCAPS-1D, *RSC Adv.*, 2024, **14**(16), 10930–10941, DOI: 10.1039/D4RA00634H.

43 H. Dixit, D. Punetha and S. K. Pandey, Improvement in performance of lead free inverted perovskite solar cell by optimization of solar parameters, *Optik*, 2019, **179**, 969–976, DOI: 10.1016/j.ijleo.2018.11.028.

44 S. P. Malyukov, A. V Sayenko and A. V Ivanova, Numerical modeling of perovskite solar cells with a planar structure, *IOP Conf. Ser.:Mater. Sci. Eng.*, 2016, **151**, 012033, DOI: 10.1088/1757-899X/151/1/012033.

45 Z. Yang, *et al.*, Enhancing electron diffusion length in narrow-bandgap perovskites for efficient monolithic perovskite tandem solar cells, *Nat. Commun.*, 2019, **10**(1), 4498, DOI: 10.1038/s41467-019-12513-x.

46 J. Cerdà, J. Arbiol, R. Diaz, G. Dezanneau and J. R. Morante, Synthesis of perovskite-type BaSnO3 particles obtained by a new simple wet chemical route based on a sol–gel process, *Mater. Lett.*, 2002, **56**(3), 131–136, DOI: 10.1016/S0167-577X(02)00428-7.

47 W. Yang, D. Zhong, M. Shi, S. Qu and H. Chen, Toward Highly Thermal Stable Perovskite Solar Cells by Rational Design of Interfacial Layer, *iScience*, 2019, **22**, 534–543, DOI: 10.1016/J.ISCI.2019.11.007.

48 J. Debgupta, *et al.*, Predictive Removal of Interfacial Defect-Induced Trap States between Titanium Dioxide Nanoparticles via Sub-Monolayer Zirconium Coating, *J. Phys. Chem. C*, 2022, **127**(1), 660–671, DOI: 10.1021/ACS.JPCC.2C06927.

49 M. S. Jamal, *et al.*, Effect of defect density and energy level mismatch on the performance of perovskite solar cells by numerical simulation, *Optik*, 2019, **182**, 1204–1210, DOI: 10.1016/j.ijleo.2018.12.163.

50 J. Haddad, *et al.*, Analyzing Interface Recombination in Lead-Halide Perovskite Solar Cells with Organic and Inorganic Hole-Transport Layers, *Adv. Mater. Interfaces*, 2020, **7**(16), 2000366, DOI: 10.1002/admi.202000366.

51 M. Noman, M. Shahzaib, S. T. Jan, S. N. Shah and A. D. Khan, 26.48% efficient and stable $FAPbI_3$ perovskite solar cells employing $SrCu_2O_2$ as hole transport layer, *RSC Adv.*, 2023, **13**(3), 1892–1905, DOI: 10.1039/D2RA06535E.

52 A. S. Chouhan, N. P. Jasti and S. Avasthi, Effect of interface defect density on performance of perovskite solar cell: Correlation of simulation and experiment, *Mater. Lett.*, 2018, **221**, 150–153, DOI: 10.1016/j.matlet.2018.03.095.

53 Z. Feng, *et al.*, Buried Interface Modulation Using Self-Assembled Monolayer and Ionic Liquid Hybrids for High-Performance Perovskite and Perovskite/CuInGaSe2 Tandem Photovoltaics, *Adv. Mater.*, 2025, **37**(8), 2412692, DOI: 10.1002/ADMA.202412692.

54 S. Wang, *et al.*, Impact of loss mechanisms on performances of perovskite solar cells, *Phys. B*, 2022, **647**, 414363, DOI: 10.1016/j.physb.2022.414363.

55 R. H. Sardar, A. Bera, S. Chattopadhyay, S. I. Ali, S. Pramanik and A. C. Mandal, The impact of series (Rs) and shunt resistances (Rsh) on solar cell parameters to enhance the photovoltaic performance of f-PSCs, *Opt. Mater.*, 2024, **155**, 115818, DOI: 10.1016/J.OPTMAT.2024.115818.

56 R. Singh, S. Sandhu and J.-J. Lee, Elucidating the effect of shunt losses on the performance of mesoporous perovskite solar cells, *Sol. Energy*, 2019, **193**, 956–961, DOI: 10.1016/j.solener.2019.10.018.

57 K. Chakraborty, M. G. Choudhury and S. Paul, Numerical study of Cs2TiX6 (X = Br−, I−, F− and Cl−) based perovskite solar cell using SCAPS-1D device simulation, *Sol. Energy*, 2019, **194**, 886–892, DOI: 10.1016/j.solener.2019.11.005.

58 F. Behrouznejad, S. Shahbazi, N. Taghavinia, H.-P. Wu and E. Wei-Guang Diau, A study on utilizing different metals as the back contact of $CH_3NH_3PbI_3$ perovskite solar cells, *J. Mater. Chem. A*, 2016, **4**(35), 13488–13498, DOI: 10.1039/C6TA05938D.

59 X. Lin, *et al.*, Dipole-field-assisted charge extraction in metal-perovskite-metal back-contact solar cells, *Nat. Commun.*, 2017, **8**(1), 613, DOI: 10.1038/s41467-017-00588-3.

60 F. Behrouznejad, S. Shahbazi, N. Taghavinia, H. P. Wu and E. Wei-Guang Diau, A study on utilizing different metals as the back contact of CH3NH3PbI3 perovskite solar cells, *J. Mater. Chem. A*, 2016, **4**(35), 13488–13498, DOI: 10.1039/C6TA05938D.

61 W. Shockley and H. J. Queisser, Detailed Balance Limit of Efficiency of p-n Junction Solar Cells, *J. Appl. Phys.*, 1961, **32**(3), 510–519, DOI: 10.1063/1.1736034.

62 A. Morales-Acevedo, Fundamentals of solar cell physics revisited: Common pitfalls when reporting calculated and measured photocurrent density, open-circuit voltage, and efficiency of solar cells, *Sol. Energy*, 2023, **262**, 111774, DOI: 10.1016/J.SOLENER.2023.05.051.